Chinese Chemical Letters 33 (2022) 1927–1932

Contents lists available at ScienceDirect

Chinese Chemical Letters

journal homepage: www.elsevier.com/locate/cclet

Precisely engineering a dual-drug cooperative nanoassembly for proteasome inhibition-potentiated photodynamic therapy

Fujun Yang[a], Qingyu Ji[a], Rui Liao[a], Shumeng Li[a], Yuequan Wang[a], Xuanbo Zhang[a], Shenwu Zhang[a], Haotian Zhang[b], Qiming Kan[b], Jin Sun[a], Zhonggui He[a], Bingjun Sun[a,*], Cong Luo[a,*]

[a] Department of Pharmaceutics, Wuya College of Innovation, Shenyang Pharmaceutical University, Shenyang 110016, China
[b] Department of Pharmacology, School of Life Science and Biopharmaceutics, Shenyang Pharmaceutical University, Shenyang 110016, China

ARTICLE INFO

Article history:
Received 7 September 2021
Revised 15 November 2021
Accepted 16 November 2021
Available online 24 November 2021

Keywords:
Bortezomib
Pyropheophorbide a
Precisely cooperative nanoassembly
Proteasome inhibition
Photodynamic therapy
Multimodal cancer therapy

ABSTRACT

Photodynamic therapy (PDT) has been widely investigated for cancer therapy. The intracellular accumulation of reactive oxygen species (ROS)-damaged protein facilitates tumor cell apoptosis. However, there is growing evidence that the ubiquitin-proteasome pathway (UPP) significantly impedes PDT by preventing the enrichment of ROS-damaged proteins in tumor cells. To tackle this challenge, we report a facile dual-drug nanoassembly based on the discovery of an interesting co-assembly of bortezomib (BTZ, a proteasome inhibitor) and pyropheophorbide a (PPa) for proteasome inhibition-mediated PDT sensitization. The precisely engineered nanoassembly with the optimal dose ratio of BTZ and PPa demonstrates multiple advantages, including simple fabrication, high drug co-loading efficiency, flexible dose adjustment, good colloidal stability, long systemic circulation, favorable tumor-specific accumulation, as well as significant enrichment of ROS-damaged proteins in tumor cells. As a result, the cooperative nanoassembly exhibits potent synergistic antitumor activity *in vivo*. This study provides a novel dual-drug engineering modality for multimodal cancer treatment.

Reactive oxygen species (ROS) generated from photosensitizers (PSs) under laser irradiation induce oxidative damages to intracellular proteins, resulting in cell apoptosis or necrosis [1,2]. However, the ubiquitin-proteasome pathway (UPP) has been found to help clear away the ROS-damaged proteins [3,4]. Given the crucial role in clearing up the intracellular oxidation-damaged proteins, UPP has been implicated as one of the main barriers in PDT [3,5]. Various proteasome inhibitors have been developed for cancer therapy [6]. Among them, bortezomib (BTZ), as the first proteasome inhibitor approved for myeloma, has also revealed potent antineoplastic activity against various human cancer cell lines [7].

There is growing evidence that BTZ-mediated proteasome inhibition has synergy effect with photodynamic PSs [3]. Based on this rationale, a precise combination of BTZ and PSs would significantly improve the sensitization of tumor cells to PDT. However, efficient co-delivery of two or more therapeutic agents remains challenging [8]. Biomedical nanotechnology has been widely applied in drug delivery [9–12]. Rational design of nanocarriers not only effectively improves the unfavorable physicochemical properties of drugs, but also achieves tumor-specific drug accumulation and on-demand drug release [13–16]. Thus, multitudinous nanocarriers such as micelles and liposomes have been designed over the past few decades. However, there are still many challenges for these conventional co-delivery nano-vehicles, including poor encapsulation stability, low co-loading efficiency, inconvenient adjustion of drug proportions and as well as premature drug leakage due to the affinity difference between carrier materials and drugs [17–19]. Therefore, carrier-free nanoassembly formed by drugs themselves has emerged as a potential nanoplatform for efficient drug delivery. In such unique nanosystems, drug molecules act as both cargos and vehicles, contributing to high drug loading efficiency and low excipient-induced side effects. More importantly, rational design of hybrid nanosystems co-assembled by two or more drugs themselves is expected to provide a versatile nanoplatform for combined drug delivery and multimodal cancer therapy [9–19].

To address these challenges, we aimed to develop a precisely chemical drug-engineered nanoassembly of BTZ and PSs for proteasome inhibition-mediated PDT sensitization (Fig. 1). Several commonly used PSs were utilized to co-assemble with BTZ (Fig. 2), including a BODIPY dye (3-bodipy-propanoic acid, BDP), two

* Corresponding authors.
E-mail addresses: sunbingjun_spy@sina.com (B. Sun), luocong@syphu.edu.cn (C. Luo).

https://doi.org/10.1016/j.cclet.2021.11.056
1001-8417/

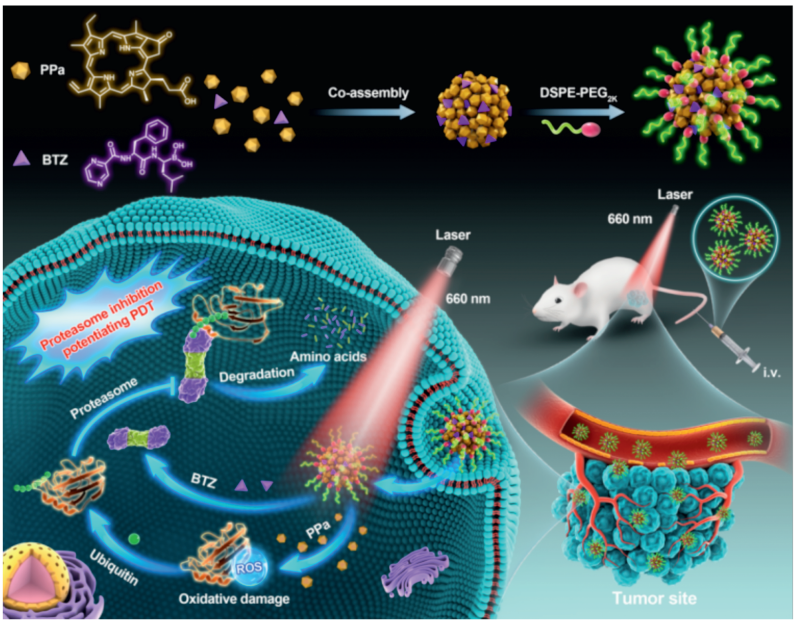

Fig. 1. Schematic representation of BTZ/PPa nanoassembly and proteasome inhibition-sensitized PDT.

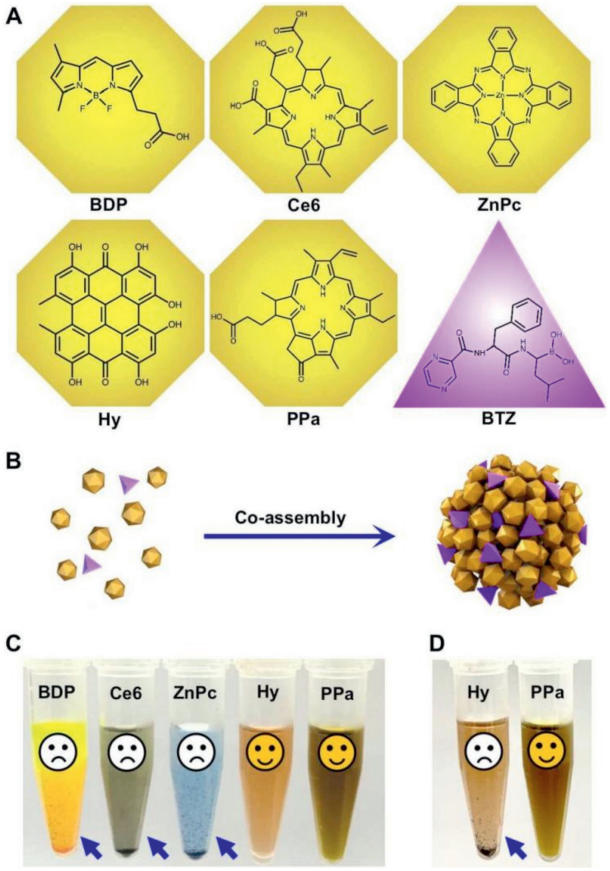

Fig. 2. Screening of co-assembly drug pair. (A) Molecular structures of five photodynamic PSs (yellow) and BTZ (purple). (B) Schematic illustration of the co-assembly process. (C) Appearance photos of the nanoassemblies at a molar ratio of 1:1. (D) Appearance photos of BTZ@Hy nanoassembly and BTZ@PPa nanoassembly at a molar ratio of 1:1 after incubation at 37 °C for 12 h.

porphyrin derivatives (Ce6 and PPa), a phthalocyanine (zinc phthalocyanine, ZnPc) and a hypericum derivative (hypericin, Hy). As shown in Figs. 2A-C and Table S1 (Supporting information), only Hy and PPa formed nanoassemblies with PPa, while BDP, Ce6 and ZnPc immediately precipitated under the same conditions. Notably, Ce6 demonstrated inferior co-assembly ability with BTZ when compared to PPa with the same porphyrin ring, due to the higher hydrophilicity of Ce6 with three carboxyl groups, resulting in weak hydrophobic force between Ce6 and BTZ. After preliminarily screening out the potential candidate PSs (PPa and Hy), we further compared the storage and colloidal stability of BTZ@PPa nanoassembly and BTZ@Hy nanoassembly. As shown in Fig. 2D, drugs precipitated from BTZ@Hy nanoassembly after incubation in a shaking table (37 °C) for 12 h. By contrast, BTZ/PPa nanoassembly revealed excellent colloidal stability under the same conditions (Fig. 2D). Based on the modular assembly optimization results, PPa and BTZ stood out as a favorable co-assembly pair for further investigation.

Moreover, the optimal synergistic dose ratio of BTZ and PPa was evaluated in 4T1 and CT26 cells at various molar ratios (5:1, 4:1, 3:1, 2:1, 1:1, 1:2, 1:3, 1:4 and 1:5). As shown in Fig. S1 and Table S2 (Supporting information), the nanoassembly of BTZ and PPa at a molar ratio of 1:4 (BTZ/PPa) exhibited the most potent cytotoxicity, with CI values of 0.38 and 0.54 in 4T1 and CT26 cells, respectively. Afterwards, the non-PEGylated nanoassembly (BTZ@PPa NPs) and PEGylated nanoassembly (BTZ@PPa PEG_{2k} NPs) were fabricated by one-step nano-precipitation approach at the optimal synergy dose ratio of 1:4 (BTZ/PPa). As shown in Fig. 3A and Table S3 (Supporting information), the mean diameter and zeta potential of BTZ@PPa NPs were approximately 88 nm and −15 mV, with impressively high drug loading capacity of BTZ (15.2 wt%) and PPa (84.8 wt%), respectively. Notably, the EE_{BTZ} and EE_{PPa} in the PEGylated nanoassembly (BTZ@PPa NPs) were up to 97.9% and 99.2% (Table S3). After PEGylation modification, the mean diameter of BTZ@PPa PEG_{2k} NPs slightly increased (103 nm, Fig. 3B). And its zeta potential reduced from around −15 mV to −22 mV, which could contribute to colloidal stability [20–22]. Moreover, BTZ@PPa PEG_{2k} NPs had a high co-loading rate for BTZ (12.2 wt%) and PPa (67.8 wt%). As expected, PEGylation decoration significantly improve the stability of BTZ@PPa nanoassembly. As illustrated in Fig. 3C, the particle size of BTZ@PPa PEG_{2k} NPs did not significantly change during the incubation with PBS supplemented with 10% FBS for 12 h, while the particle size of BTZ@PPa NPs significantly increased under the same conditions.

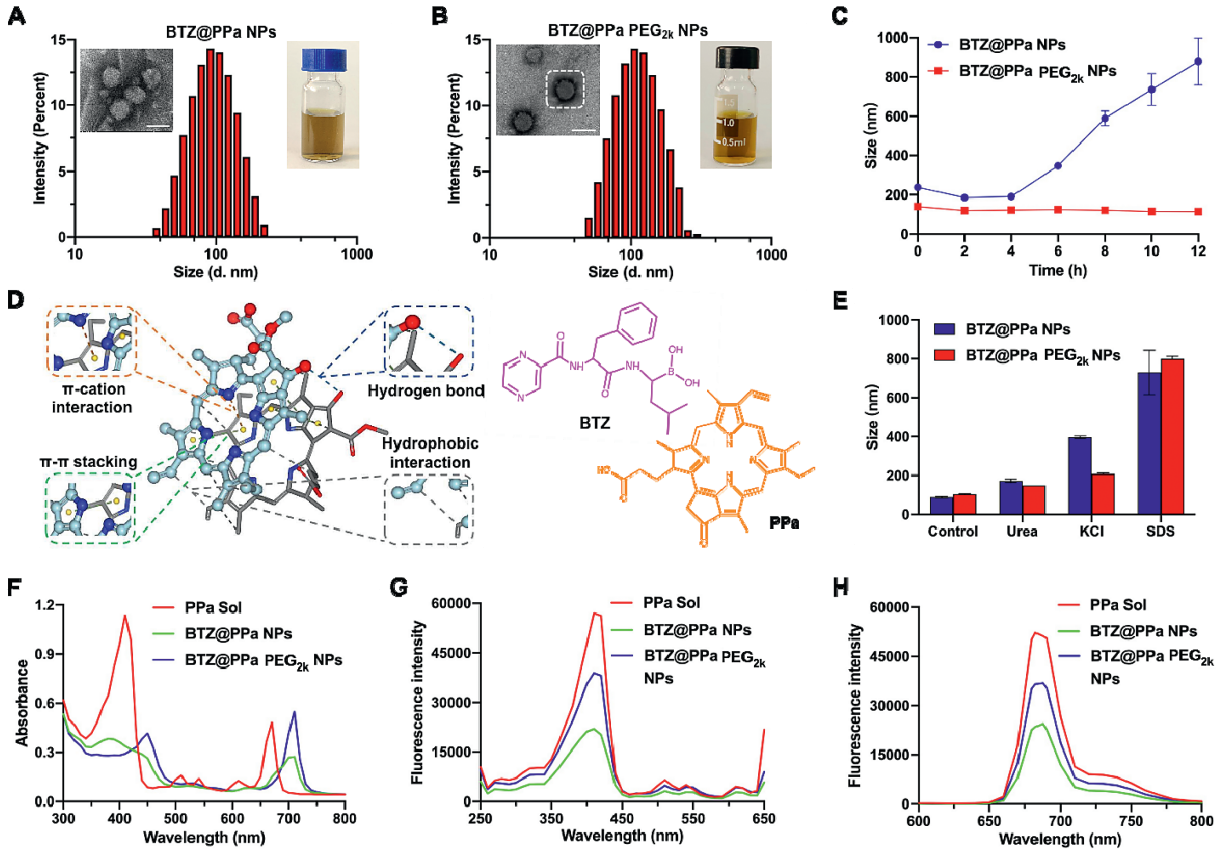

Fig. 3. Characterization of the co-assembled NPs. (A and B) Intensity size distribution profiles, TEM images and appearance photographs. Scale bar: 100 nm. (C) Colloidal stability ($n = 3$). (D) Molecular dynamics simulation results. (E) The particle size changes of NPs treated with urea, SDS and KCl (200 mmol/L). (F) UV absorption spectra at 300–800 nm. (G) The PPa fluorescence spectra from 250 nm to 650 nm. (H) The PPa fluorescence spectra of PPa Sol, BTZ@PPa NPs and BTZ@PPa PEG_{2k} NPs from 600 nm to 800 nm.

We then explored the intermolecular interactions using computational docking simulation technique. As shown in Fig. 3D, there were four interactions or forces found between BTZ and PPa, including π-cation interaction, π-π stacking interaction, hydrophobic force and hydrogen bond. We further validated these intermolecular interactions by utilizing three destructive agents (KCl, urea and SDS), which have been widely employed to break intermolecular π-cation interaction, hydrogen bond and hydrophobic force, respectively [23–25]. Moreover, π-π stacking interaction was verified by scanning the UV absorbance spectra of PPa before and after co-assembly with BTZ. As illustrated in Fig. 3E, the particle size of both BTZ@PPa NPs and BTZ@PPa PEG_{2k} NPs increased after the incubation with these destructive agents, confirming a comprehensive contribution of π-action interaction, hydrogen bond and hydrophobic force to the co-assembly process. In addition, obvious red-shift was observed in the UV spectra of PPa in nanoassemblies when compared with PPa solution (Fig. 3F), indicating the existence of the π-π stacking interaction in the nanoassembly. Moreover, significant fluorescence spectra changes of PPa were observed before and after co-assembly with BTZ. As shown in Figs. 3G and H, the fluorescence intensity of PPa decreased after co-assembly with BTZ, which should be ascribed to the aggregation caused quench (ACQ) effect of PPa in the state of aggregation [26–28].

We then explored the *in vitro* release patterns of BTZ with or without light treatment (660 nm, 50 mW/cm^2, 5 min). As shown in Fig. S2 (Supporting information), the PEGylated nanoassembly (BTZ@PPa PEG_{2k} NPs) demonstrated sustained release behaviors in contrast to BTZ Sol and BTZ@PPa NPs, with less than 30% of BTZ released from the nanoassemblies. Notably, owing to the disintegration of nanostructures following the photobleaching damage on PPa, laser irradiation significantly accelerated BTZ release from BTZ@PPa PEG_{2k} NPs. The sustained-release behavior of nanoassembly favor safe drug delivery, and the tumor-localized rapid release of BTZ promoted by laser irradiation could certainly potentiate synergistic therapeutic effect.

The cellular uptake of nanoassemblies was investigated in 4T1 cells. As shown in Figs. 4A-D, PPa Sol, BTZ@PPa NPs and BTZ@PPa PEG_{2k} NPs were internalized into tumor cells in a time-dependent way. Notably, BTZ@PPa PEG_{2k} NPs demonstrated much higher cellular uptake efficiency than that of PPa Sol and BTZ@PPa NPs under the same conditions, especially at 4 h. The favorable cellular uptake of BTZ@PPa PEG_{2k} NPs could be attributed to its good colloidal stability (Fig. 3C). By contrast, there's no significant difference observed in the cellular uptake of PPa Sol and BTZ@PPa NPs. The inferior cellular internalization of the non-PEGylated BTZ@PPa NPs should be ascribed to its poor stability (Fig. 3C).

We then explored the cellular ROS generation ability of nanoassemblies with/no laser irradiation (660 nm) in 4T1 cells. As depicted in Fig. 4E, the cells treated with PPa Sol, BTZ@PPa NPs and BTZ@PPa PEG_{2k} NPs showed much stronger fluorescence signals under laser irradiation (50 mW/cm^2, 5 min) than that of the cells without laser treatment, suggesting the excellent cellular ROS generation ability of PPa under laser irradiation. Notably, there is almost no significant fluorescence difference among the cells receiving PPa Sol, BTZ@PPa NPs and BTZ@PPa PEG_{2k} NPs, suggesting the comparable cellular ROS generation capacity of PPa Sol and nanoassemblies (Fig. 4E). Given that the nanostructure of BTZ@PPa

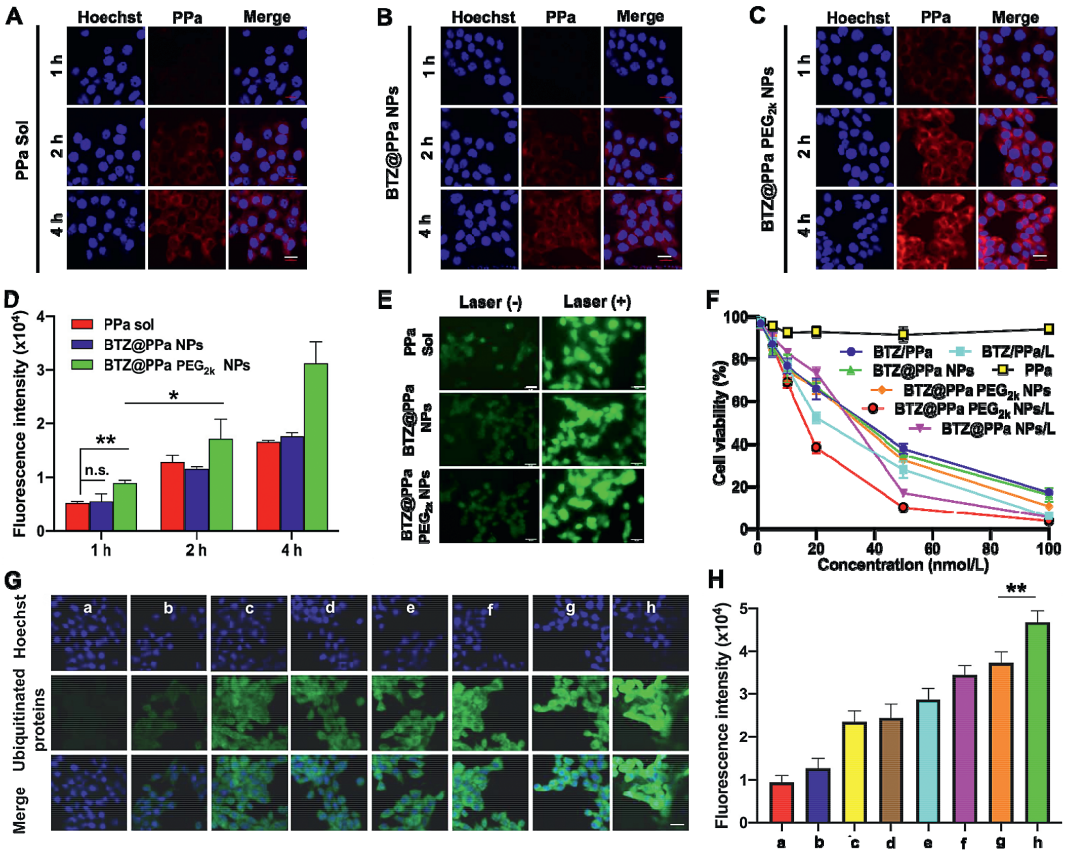

Fig. 4. Cellular uptake, ROS generation, synergistic cytotoxicity and proteasome inhibition of nanoassemblies. (A-C) Cellular uptake at a PPa equivalent dose of 2.5 μg/mL by CLSM at 1, 2 and 4 h. Scale bar: 50 nm. (D) Quantitative analysis of cellular fluorescence intensity. (E) Cellular ROS generation in 4T1 cells at an equivalent PPa dose of 100 nmol/L with/without laser irradiation (660 nm, 50 mW/cm^2, 5 min). (F) Synergistic cytotoxicity of various formulations in 4T1 cells with/without laser irradiation (660 nm, 50 mW/cm^2, 5 min). (G) Immunofluorescence (Scale bar: 50 nm) and (H) quantitative analysis of the ubiquitinated proteins in 4T1 cells at a PPa equivalent of 100 nmol/L with/no laser irradiation (660 nm, 50 mW/cm^2, 5 min), a, b, c, d, e, f, g and h represent saline, PPa/L, BTZ, BTZ@PPa NPs, BTZ@PPa PEG$_{2k}$ NPs, BTZ@PPa NPs/L, BTZ/PPa/L and BTZ@PPa PEG$_{2k}$ NPs/L, respectively. n.s., no significance; $^*P < 0.05$, $^{**}P < 0.01$.

NPs would be rapidly disintegrated by salts and FBS in cell culture media, it is understandable that BTZ@PPa NPs revealed similar cellular uptake and cellular ROS generation efficiency with PPa Sol. By contrast, despite the ACQ effect of PPa in BTZ@PPa PEG$_{2k}$ NPs (Figs. 3G and H), favorable colloidal stability and efficient cellular uptake endowed the PEGylated nanoassembly with high cellular ROS generation capacity.

The favorable colloidal stability, cellular uptake and ROS generation of BTZ@PPa PEG$_{2k}$ NPs inspired us to further study the synergistic cytotoxicity of BTZ and PPa. As shown in Fig. 4F and Fig. S3 (Supporting information), the laser irradiated groups revealed higher cytotoxicity than that of the groups without laser treatment, suggesting the proteasome inhibition-sensitized photodynamic cytotoxicity. Notably, BTZ@PPa PEG$_{2k}$ NPs with laser irradiation exhibited the strongest synergistic cytotoxicity, which could be ascribed to the rational dose ratio, good colloidal stability, efficient cellular uptake, as well as favorable ROS generation capacity of the PEGylated nanoassembly.

We then investigated the *in vitro* synergistic mechanisms of proteasome inhibition-mediated PDT sensitization by evaluating the enrichment of ubiquitinated proteins in 4T1 cells. As shown in Figs. 4G and H, laser-irradiated groups significantly facilitated the enrichment of the ubiquitinated proteins in tumor cells. BTZ alone also induce the production of the ubiquitinated proteins. These results indicated that the ROS generated by PPa under laser irradiation exerted oxidative damages on proteins, and BTZ synergistically prevented the clearance of these destructed proteins. Notably, BTZ@PPa PEG$_{2k}$ NPs induced significant accumulation of the ubiquitinated proteins in tumor cells under laser irradiation, which was in consist with the cytotoxicity outcomes (Fig. 4F). These results confirmed our hypothesis that precise integration of BTZ and PPa into one nanosystem could realize proteasome inhibition-mediated PDT sensitization.

All the animal experiments were approved by the Animal Ethics Committee of Shenyang Pharmaceutical University. The pharmacokinetic profiles of PPa Sol, BTZ@PPa NPs and BTZ@PPa PEG$_{2k}$ NPs were investigated in SD rats. As depicted in Fig. S4 (Supporting information), PPa Sol was rapidly cleared from the blood after intravenous administration, owing to the short half-life of free drugs. Moreover, the non-PEGylated BTZ@PPa NPs revealed similar pharmacokinetics behavior with PPa Sol, due to its poor colloidal stability. Notably, the $C_{0.5}$ value (850.6 ± 70.8 ng/mL) of BTZ@PPa NPs was less than that of PPa Sol (1370.5 ± 142.5 ng/mL), indicating the rapid clearance of the non-PEGylated nanoassembly by the RES system in the body. As expected, BTZ@PPa PEG$_{2k}$ NPs significantly extended the circulation time in the blood (Fig. S4 and Table S3). Long circulation of NPs certainly facilitates the tumor-specific accumulation via the enhanced permeability and retention (EPR) effect [29]. As shown in Figs. S4 and S5 (Supporting information), the accumulation of PPa Sol, BTZ@PPa NPs and BTZ@PPa PEG$_{2k}$ NPs in the major organs (heart, liver, spleen, lung and kidney) and tumors presented an earlier increase and later decrease trend from 2 h to 24 h, and the peak drug accumulation in tumors was found at around 4 h post-injection for all these formulations. Moreover, the fluorescent signals in the major organs and tumors significantly decreased at 12 and 24 h after intravenous

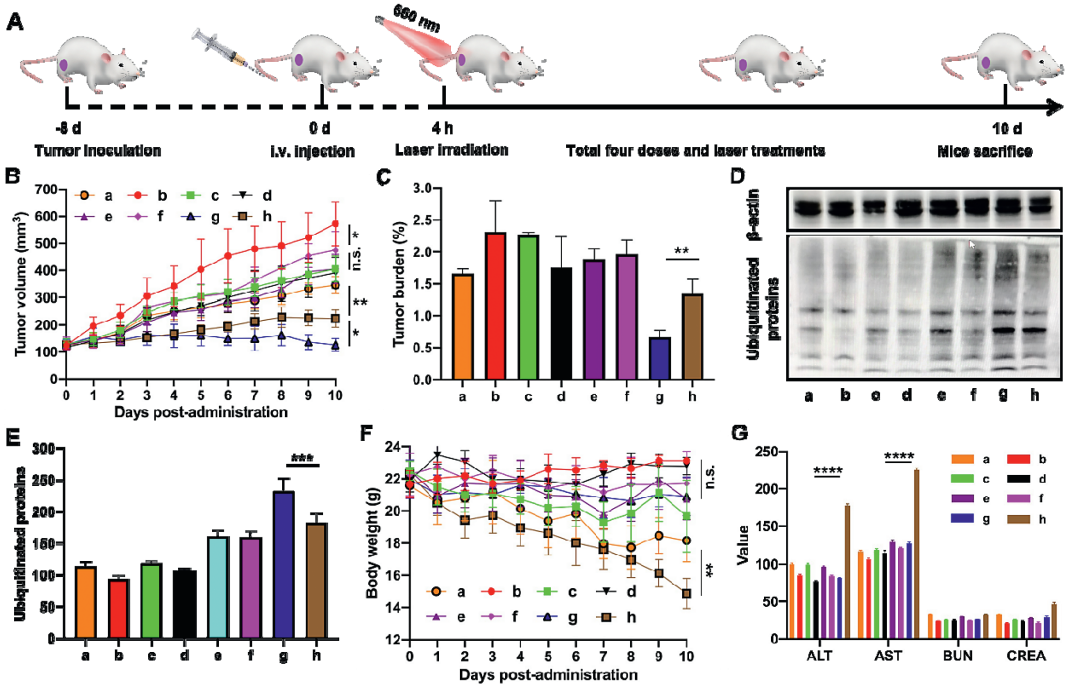

Fig. 5. *In vivo* proteasome inhibition-potentiated PDT against 4T1 breast cancer ($n = 6$). (A) Experimental design. (B) Tumor growth curves. (C) Tumor burden. (D) Western blot results of the ubiquitinated proteins expression in tumor tissues. (E) Quantification of the relative ubiquitinated proteins. (F) Body weight changes. (G) Hepatorenal function evaluation (AST: aspartate aminotransferase (U/L); ALT: alanine aminotransferase (U/L), BUN: blood urea nitrogen (mg/dL), CREA: creatinine (μmol/L)). The a, b, c, d, e, f, g and h represent BTZ Sol, saline, BTZ@PPa NPs, PPa/L, BTZ@PPa NPs/L, BTZ@PPa PEG_{2k} NPs, BTZ@PPa PEG_{2k} NPs/L and BTZ/PPa/L, respectively.

administration, which was consistent with the pharmacokinetics results (Fig. S4). Notably, BTZ@PPa PEG_{2k} NPs showed much higher tumor accumulation when compared with PPa Sol and BTZ@PPa NPs (Fig. S4), which should be attributed to its excellent colloidal stability and long circulation time in the blood

The *in vivo* proteasome inhibition-potentiated PDT was evaluated against a triple-negative breast cancer xenograft tumor model (Fig. 5A). According to the *ex vivo* biodistribution results (Figs. S5 and S6 in Supporting information), the laser-treated groups were exposed to laser irradiation (660 nm, 50 W/cm^2) for 5 min at 4 h post-administration. As shown in Figs. 5B and C, the tumor growth of laser-treated groups was slower than that of the groups without laser irradiation. BTZ/PPa/L (g) group showed stronger antitumor activity than that of BTZ Sol (a) and PPa Sol/L (d), suggesting the synergy effect of BTZ-mediated chemotherapy and PPa-based PDT. Notably, the non-PEGylated BTZ@PPa NPs (c and e) showed inferior antitumor activity even with laser treatment, which should be ascribed to its poor colloidal stability and rapid clearance from the body after administration (Table S4 in Supporting information). As expected, BTZ@PPa PEG_{2k} NPs demonstrated the most potent antitumor activity under laser irradiation (Figs. 5B and C, and Fig. S7 in Supporting information), due to the prominent advantages in the whole drug delivery process, including good colloidal stability, long systemic circulation (Fig. S4), high tumor accumulation (Fig. S5), favorable cellular uptake (Figs. 4A-C), as well as efficient ROS generation (Fig. 4E). After the final treatment, the cellular apoptosis of tumor was assessed by TUNEL and Ki67 assay. As shown in Figs. S8A and B (Supporting information), BTZ@PPa PEG_{2k} NPs caused large apoptosis and small proliferation. Additionally, the expression of ubiquitinated proteins in tumor tissues after treatments was further evaluated to investigate proteasome inhibition *in vivo*. As shown in Figs. 5D and E, BTZ@PPa PEG_{2k} NPs significantly increased the ubiquitinated proteins in tumors under laser irradiation when compared with other therapeutic modalities.

As previously mentioned, despite the potent cytotoxicity of BTZ against multiple tumor cell lines, it also causes serious off-target toxicity [30,31]. We expected that precisely formulating BTZ and PSs into one nanosystem would not only achieve synergistic antitumor effect, but also is expected to significantly reduce the off-target toxicity of BTZ. As shown in Fig. 5F, obvious weight loss was found in the groups of BTZ Sol and BTZ/PPa/L, indicating the severe systemic toxicity of BTZ. Besides, notable reduction of the spleen size provided further evidence of BTZ-induced organ toxicity (Fig. S9 in Supporting information). Moreover, the hepatic and renal function indicators also revealed the obvious toxicity of BTZ/PPa/L to liver (Fig. 5G). By contrast, precisely formulating BTZ and PPa into dual-drug hybrid nanoassembly (BTZ@PPa PEG_{2k} NPs) show almost no systemic toxicity during the treatment process (Figs. 5F and G). Moreover, there was no distinct histological variation found in the H&E staining sections of heart, liver, spleen, lung and kidney (Fig. S10 in Supporting information).

In summary, inspired by the synergy between ubiquitin-proteasome pathway and ROS-induced protein destruction, we developed a facile nanoassembly of BTZ and PPa after modular assembly and synergistic cytotoxicity optimization. Multiple intermolecular interactions and forces were found to drive the dual-drug co-assembly. The PEGylated nanoassembly (BTZ@PPa PEG_{2k} NPs) with an optimal dose ratio of 1:4 (BTZ/PPa) demonstrated distinct advantages throughout the whole drug delivery process, resulting in potent synergistic antitumor effect in a triple-negative breast tumor xenograft mouse model. Proteasome inhibition-sensitized PDT was observed in cellular and whole-animal levels.

Declaration of competing interest

The authors declare that they have no known competing financial interests or personal relationships that could have appeared to influence the work reported in this paper.

Acknowledgments

This work was financially supported by the Liaoning Revitalization Talents Program (No. XLYC1907129), the Excellent Youth Science Foundation of Liaoning Province (No. 2020-YQ-06), and the China Postdoctoral Science Foundation (No. 2020M670794).

Supplementary materials

Supplementary material associated with this article can be found, in the online version, at doi:10.1016/j.cclet.2021.11.056.

References

[1] B. Sun, Y. Chen, H. Yu, et al., Acta Biomater 92 (2019) 219–228.
[2] S. Li, F. Yang, X. Sun, et al., Chem. Eng. J. (2021) 130838.
[3] A. Szokalska, M. Makowski, D. Nowis, et al., Cancer Res. 69 (2009) 4235–4243.
[4] Q. Wang, M. Sun, D. Li, et al., Theranostics 10 (2020) 5550–5564.
[5] M.M. Hiller, A. Finger, M. Schweiger, et al., Science 273 (1996) 1725–1728.
[6] A. Mani, E.P. Gelmann, J. Clin. Oncol. 23 (2005) 4776–4789.
[7] S. Shen, X.J. Du, J. Liu, et al., J. Control. Release 208 (2015) 14–24.
[8] C. Luo, B. Sun, C. Wang, et al., J. Control. Release 302 (2019) 79–89.
[9] N. Ahmed, H. Fessi, A. Elaissari, Drug Discov. Today 17 (2012) 928–934.
[10] K. Ding, C. Zheng, L. Sun, et al., Chin. Chem. Lett. 31 (2020) 1168–1172.
[11] H. Yu, T. Man, W. Ji, et al., Chin. Chem. Lett. 30 (2019) 175–178.
[12] W. Zhang, F. Wang, C. Hu, et al., Acta Pharm. Sin. B 10 (2020) 2037–2053.
[13] F. Yang, Z. Zhao, B. Sun, et al., Trends Cancer 6 (2020) 645–659.
[14] S. Li, X. Shan, Y. Wang, et al., J. Control. Release 326 (2020) 510–522.
[15] L. Tian, Y. Ma, M. Li, et al., Chin. Chem. Lett. 31 (2020) 1159–1161.
[16] J. Hu, X. Yuan, F. Wang, et al., Chin. Chem. Lett. 32 (2021) 1341–1347.
[17] X. Zhang, J. Xiong, K. Wang, et al., Bioact. Mater. 6 (2021) 2291–2302.
[18] W. Zhang, J. Shen, H. Su, et al., ACS Appl. Mater. Interfaces 8 (2016) 13332–13340.
[19] C. Luo, J. Sun, B. Sun, et al., Trends Pharmacol. Sci. 35 (2014) 556–566.
[20] C. Luo, J. Sun, B. Sun, et al., Small 12 (2016) 6353–6362.
[21] C. Luo, J. Sun, D. Liu, et al., Nano Lett. 16 (2016) 5401–5408.
[22] X. Shan, X. Zhang, C. Wang, et al., J. Nanobiotechnol. 19 (2021) 1–13.
[23] H.R. Jia, Y.X. Zhu, K.F. Xu, et al., Adv. Healthc. Mater. 7 (2018) e1800380.
[24] Y.X. Zhu, H.R. Jia, G.Y. Pan, et al., J. Am. Chem. Soc. 140 (2018) 4062–4070.
[25] F. Aydin, A. Moradzadeh, C.L. Bilodeau, et al., J. Chem. Theory Comput. 17 (2021) 1596–1605.
[26] X. Hu, X. Dong, Y. Lu, et al., Drug Discov. Today 22 (2017) 382–387.
[27] Z. Zhu, J. Qian, X. Zhao, et al., ACS Nano 10 (2016) 588–597.
[28] C. Ren, H. Wang, D. Mao, et al., Angew. Chem. 127 (2015) 4905–4909.
[29] K. Greish, in: Enhanced Permeability and Retention (EPR) Effect For Anticancer Nanomedicine Drug targeting, Cancer nanotechnology, Springer, 2010, pp. 25–37.
[30] T. Bao, R. Zhang, A. Badros, et al., Pain Res. Treat 2011 (2011) 920807.
[31] M.P. Giannoccaro, V. Donadio, C.Gomis Perez, et al., Neurol. Sci. 32 (2011) 361–363.